physica status solidi pss rrl
www.pss-rapid.com

Intrinsic Magnetism and Field-Driven Spin Alignment in NiI_2 Revealed by X-ray Magnetic Spectroscopy

Ethan L. Arnold, Emily Heppell, Rabindra Basnet, Binshuo Zhang, Jieyi Liu, Javier Herrero-Martín, Charles Guillemard, Yanfeng Guo, Jin Hu, Dirk Backes, Gerrit van der Laan, and Thorsten Hesjedal**

This study investigates the intrinsic magnetism and field-driven spin alignment in NiI_2 using X-ray absorption spectroscopy and X-ray magnetic circular dichroism (XMCD). NiI_2, a van der Waals material, exhibits helimagnetic and type-II multiferroic behavior. This study reveals robust XMCD signals across paramagnetic, antiferromagnetic, and helimagnetic phases under applied out-of-plane fields up to 6 T, while no net moment emerges at zero field. Atomic multiplet calculations confirm a covalent Ni 3*d* ground state with a significantly reduced spin moment. The results establish the intrinsic nature of NiI_2's magnetism and clarify its field-driven spin alignment mechanism. This comprehensive spectroscopic characterization lays the foundation for future applications of NiI_2 in advanced spintronic and multiferroic devices, despite challenges posed by its low transition temperature in the monolayer limit. Future research should focus on enhancing its critical temperature through doping, strain engineering, or heterostructure fabrication.

1. Introduction

Magnetic van der Waals (vdW) semiconductors hold great promise for future spintronic and multiferroic technologies[1,2] due to their intrinsic magnetism persisting down to the monolayer limit[3–5] and their tunability via external stimuli such as magnetic fields, strain, and electric fields.[6–8] Among these materials, nickel diiodide (NiI_2) stands out for its rich magnetic phase diagram and unique multiferroic properties.[9] At room temperature, bulk NiI_2 is paramagnetic, but upon cooling, it undergoes a series of intriguing magnetic transitions—first to an antiferromagnetic state below 75 K, and subsequently to a helimagnetic phase below 59 K. The latter transition involves a rhombohedral-to-monoclinic structural distortion, enabling an inversion-symmetry-breaking spin spiral that couples magnetism and electric polarization.[10,11] Consequently, NiI_2 is classified as an improper type-II multiferroic, with multiferroicity extending down to monolayer thickness,[12] albeit at a reduced critical temperature of around 21 K, highlighting the crucial role of dimensionality.[5]

Recent research has confirmed that exfoliated NiI_2 retains strong magnetic correlations in its 2D limit, exhibiting phenomena such as chiral magnetoelectric oscillations,[13] electromagnons,[5,14,15] and quantum-entangled magnetic states.[8] These properties position NiI_2 as an ideal candidate for applications in advanced spin-based devices.[3,4] Despite significant interest, a detailed spectroscopic characterization of the electronic and magnetic ground states of NiI_2 is still lacking.

E. L. Arnold, E. Heppell, J. Liu, T. Hesjedal
Department of Physics
Clarendon Laboratory
University of Oxford
Oxford OX1 3PU, UK
E-mail: thorsten.hesjedal@physics.ox.ac.uk

E. L. Arnold, E. Heppell, J. Liu, D. Backes, G. van der Laan, T. Hesjedal
Diamond Light Source
Harwell Science and Innovation Campus
Didcot OX11 0DE, UK
E-mail: gerrit.vanderlaan@diamond.ac.uk

The ORCID identification number(s) for the author(s) of this article can be found under https://doi.org/10.1002/pssr.202500130.

DOI: 10.1002/pssr.202500130

E. Heppell
Rutherford Appleton Laboratory
ISIS
Harwell Science and Innovation Campus
Didcot OX11 0QX, UK

R. Basnet, J. Hu
Department of Physics
Institute for Nanoscience and Engineering
University of Arkansas
Fayetteville, AR 72701, USA

B. Zhang, Y. Guo
School of Physical Science and Technology and Shanghai Tech Laboratory for Topological Physics
ShanghaiTech University
Shanghai 201210, China

J. Herrero-Martín, C. Guillemard
ALBA Synchrotron
Carrer de la Llum 2-26, Cerdanyola del Vallès 08290, Barcelona, Spain

In this work, we bridge this gap by providing a comprehensive X-ray absorption spectroscopy (XAS) and X-ray magnetic circular dichroism (XMCD) study of bulk NiI_2 single crystals as a function of temperature and applied magnetic field. Our experimental results, supported by atomic multiplet calculations, clarify the intrinsic nature of NiI_2's magnetism and lay the foundation for the future use of its unique magnetoelectric phenomena in advanced 2D heterostructures.

2. Experimental Section

At room temperature, NiI_2 adopts the $CdCl_2$-type ($R\bar{3}m$) crystal structure, shown in **Figure 1**, featuring Ni^{2+} ions arranged on triangular planes separated by I^- layers. These I^--Ni^{2+}-I^- triple slabs stack along the *c*-axis, with neighboring layers bound by weak vdW interactions.

The NiI_2 crystal was grown using chemical vapor transport. Owing to NiI_2's hygroscopic nature, which results in rapid degradation in air, the crystal was cleaved at the beamline right before the measurements in an Ar glove box that is directly interfaced with the ultrahigh vacuum (UHV) end station, thus ensuring that the sample remained in an inert environment throughout the transfer process. The sample was oriented such that the c-axis was in the out-of-plane (OOP) direction. The sample was transferred to the XMCD end-station in UHV, thus limiting degradation as far as possible. Note that the XMCD spectra show no signs of Ni oxide, indicating that there has been no deterioration of the sample.

XAS and XMCD offer the most direct way to determine the local electronic and magnetic structure of 3*d* transition metals due to their element-, valence-, site-, and symmetry-selectivity.[16] In particular, XMCD—defined as the difference between X-ray absorption spectra for photons with left and right circular polarization—enables a direct, quantitative assessment of spin and orbital moments via the well-established sum rules.[17] The XAS and XMCD measurements reported here were carried out at the BOREAS beamline at the ALBA Synchrotron (Barcelona, Spain), spanning temperatures from 2 to 300 K in a superconducting magnet. All data were collected in the total electron yield (TEY) mode, which is surface-sensitive with a typical probing depth of ≈4 nm. The incident X-ray beam was along the applied field.

Atomic multiplet calculations were performed to obtain the Ni $L_{2,3}$ XAS and XMCD spectra for the electric-dipole transitions, $3d^n \rightarrow 2p^5 3d^{n+1}$, with the spin-orbit and electrostatic interactions treated on an equal footing.[18,19] The wave functions of the initial- and final-state configurations were calculated in intermediate coupling using Cowan's atomic Hartree–Fock (HF) code with relativistic corrections.[18,20] The atomic electrostatic interactions included the 3*d*–3*d* and 2*p*–3*d* Coulomb and exchange interactions, which were reduced to 80% of their atomic HF value to account for intra-atomic screening. An octahedral crystal field of $10Dq = 2$ eV was included, which splits the 3*d*-orbitals in states of e_g and t_{2g} symmetry. Hybridization in a cluster-model mixes the $3d^{n+1}\underline{L}$ and $3d^n$ wave functions, where $\underline{L}$ represents a hole on the neighboring atoms in states of appropriate symmetry. Specifically, for NiI_2, the hybridization parameter $T = \langle \Psi(d^n)|H|\Psi(d^{n+1}\underline{L})\rangle$ was taken as $T(e_g) = 1.5$ and $T(t_{2g}) = 0.75$ eV. The relative values of the average energy of the configurations in the initial state were taken as $E(3d^8) = 0$, $E(3d^9\underline{L}) = -1.5$, and $E(3d^{10}\underline{L}^2) = 5$ eV and those in the final state as $E(2p^5 3d^9) = 0$ and $E(2p^5 3d^{10}\underline{L}) = -2.5$ eV. This resulted in a high spin $^3A_{2g}$ ground state with 54.8% d^8, 43.4% d^9, and 1.8% d^{10} character, yielding a *d*-count of $n_d = 8.47$—in good agreement with earlier performed Anderson impurity model calculations for the XAS of Ni dihalides and NiO.[21] The computed Ni L_3 (L_2) line spectra were convoluted by a Lorentzian with a half width of $\Gamma = 0.2$ eV (0.6 eV) for intrinsic lifetime broadening and a Gaussian with a standard deviation of $\sigma = 0.15$ eV for instrumental broadening.

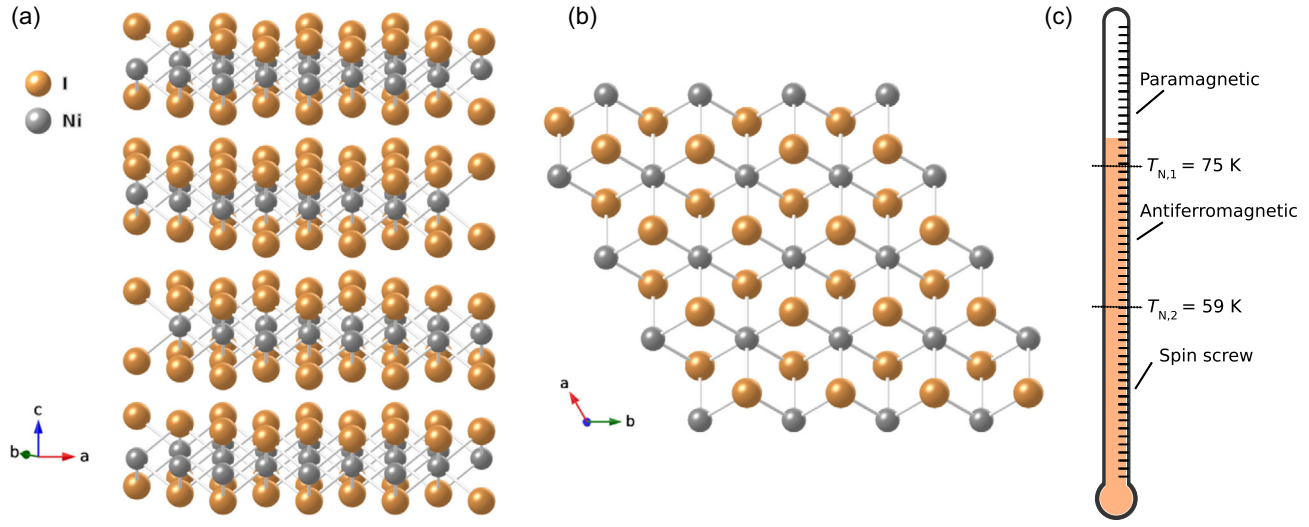

Figure 1. Crystal structure and magnetic phase diagram of NiI_2. a) At room temperature, NiI_2 adopts a $CdCl_2$-type structure (space group $R\bar{3}m$), comprising alternating layers of Ni^{2+} and I^- ions, weakly coupled via vdW interactions. b) Top–down view of the crystal structure along the *c*-axis, highlighting its triangular symmetry. c) Temperature-dependent magnetic phase diagram illustrating NiI_2's transition from a paramagnetic state at room temperature to an antiferromagnetic phase below 75 K, followed by a helimagnetic phase emerging below 59 K.

We note that the magnetic transition into the helimagnetic phase is accompanied by a structural distortion from rhombohedral to monoclinic symmetry, as reported in earlier work.[10,11] While our XMCD measurements do not directly track changes in lattice parameters, these structural modifications likely play a role in the evolution of the magnetic ground state. A detailed temperature-dependent structural analysis would be a valuable complement to the present study.

3. Results and Discussion

We begin by comparing the experimental and calculated XAS and XMCD at 65 K in a 6 T out-of-plane magnetic field, as shown in **Figure 2**. The primary peaks at the L_3 and L_2 edges, located at 851.6 and 868.7 eV, respectively, are dominated by the $2p^5 3d^{10}\underline{L}$ configuration, whereas the satellite structure at ≈3.5 eV higher photon energy corresponds mainly to $2p^5 3d^9$, split by ≈2 eV due to the core-valence exchange interaction. In the XMCD spectrum, the satellite structure displays a characteristic (−,+) signature. The spectral structure is markedly different from a pure $3d^8$ ground state, as reported in ref. [22], and instead aligns well with earlier work on Ni metal for which an impurity-model analysis revealed a significantly hybridized Ni $3d$ ground state.[23] The strong agreement between the experimental and calculated XAS confirms the high quality of the NiI_2 crystal and establishes that the XMCD signals originate from NiI_2 itself, rather than from spurious nickel metal impurities or other contamination. The observed step in the XAS intensity at ≈858 eV corresponds to the onset of the L_3 continuum states,[21] which are not taken into account in the calculation and which show no dichroism.

The element-specific spin and orbital magnetic moments were obtained from the integrated intensities of the dichroic spectra using the XMCD sum rule analysis.[24] Consider the integrated XMCD spectra, with p and q the integrated intensities over the L_3 and $L_{2,3}$ edges, respectively. Using the integrated intensity r over the $L_{2,3}$ edge of the sum spectrum as the normalization factor accounting for the number of d holes $n_h = (10 - n_d) = 1.53$, the spin and orbital moments per atom are then given by $m_L = -\langle L_Z \rangle = -(4/3)qn_h/r$ and $m_S = -\langle 2S_{eff,z} \rangle = -(6p - 4q)n_h/r$.[16] For the calculated spectra, we obtain $m_L = 0.103\ \mu_B$/Ni and $m_S = 1.36\ \mu_B$/Ni, yielding $m_L/m_S = 0.076$. By contrast, sum rule analysis on the experimental data at 65 K and 6 T (as shown in Figure 2), after background subtraction, give $m_L = 0.005\ \mu_B$/Ni and $m_S = 0.08\ \mu_B$/Ni, yielding $m_L/m_S = 0.063$. Although the ratio of orbital to spin moment, m_L/m_S, is comparable in both cases, i.e., a 17% difference, the spin moment observed experimentally is ≈17 times smaller than in the theoretical calculation. Such a strong reduction is expected and arises from the geometrical projection of the spin moment along the direction of the incoming X-ray beam. In zero field, the antiferromagnetic or helical spin textures in NiI_2 result in no net magnetization along any fixed axis, thereby suppressing the XMCD signal. Even under finite field, unless full spin alignment is achieved, only the projected component contributes to the dichroic signal. Thus, the apparent discrepancy reflects the noncollinearity of the spin structure rather than a fundamental disagreement in moment size. A detailed quantitative analysis of this reduction would require modeling the spin texture and its projection along the beam, which goes beyond the current multiplet framework.

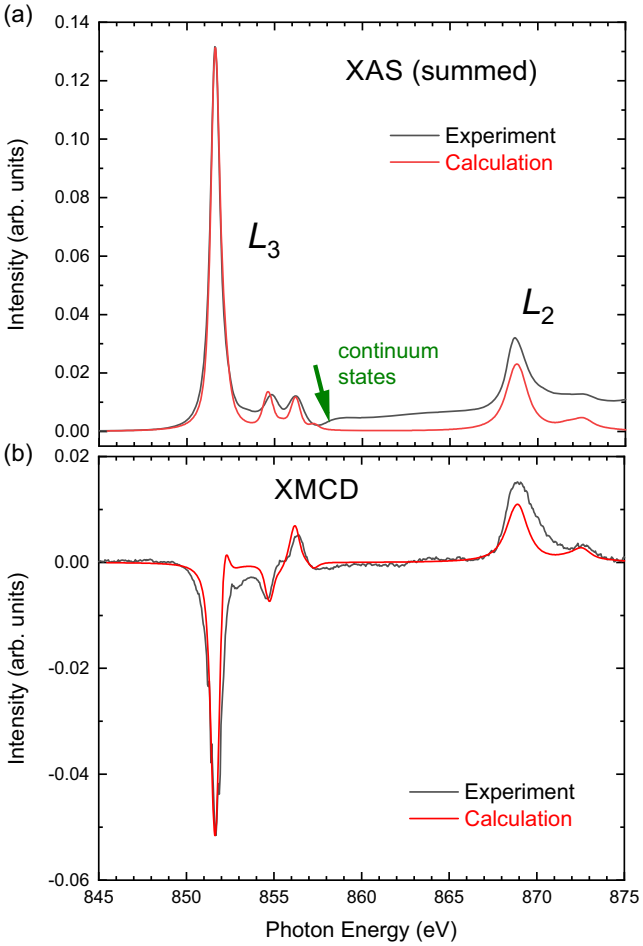

Figure 2. Comparison between experimental and calculated a) XAS, averaged over both polarizations, and b) XMCD spectra at the Ni $L_{2,3}$ edge of NiI_2. The experimental data were collected at 65 K in an out-of-plane magnetic field of 6 T in normal incidence using TEY mode. The theoretical spectra were calculated in intermediate coupling using Cowan's atomic Hartree–Fock code with relativistic corrections. Transitions to the continuum states, showing a step-like onset at ≈858 eV, as indicated by the green arrow, were not included in the calculation. The experimental XAS and XMCD spectra have been scaled to the calculated spectra in order to allow for a better comparison of the multiplet structure. To do this, the experimental XMCD intensity had to be multiplied by a factor ≈20 compared to the experimental XAS intensity. The need to scale reflects the fact that the atomic multiplet model assumes fully aligned moments and does not account for the antiferromagnetic or helical spin structures present in NiI_2.

Next, we examine the XMCD as a function of temperature. **Figure 3** shows the XMCD spectra at temperatures from 2 to 300 K, in an out-of-plane field of 6 T. The XAS spectra are normalized such that the sum of both circular polarizations has an L_3 peak intensity of unity. At lower temperatures, the XMCD spectra exhibit noticeable linewidth broadening, which is not observed in the corresponding XAS data. Moreover, the XMCD peak intensity diminishes with decreasing temperature, suggesting partial suppression of the net spin alignment, possibly due to enhanced spin-orbit interactions or domain effects

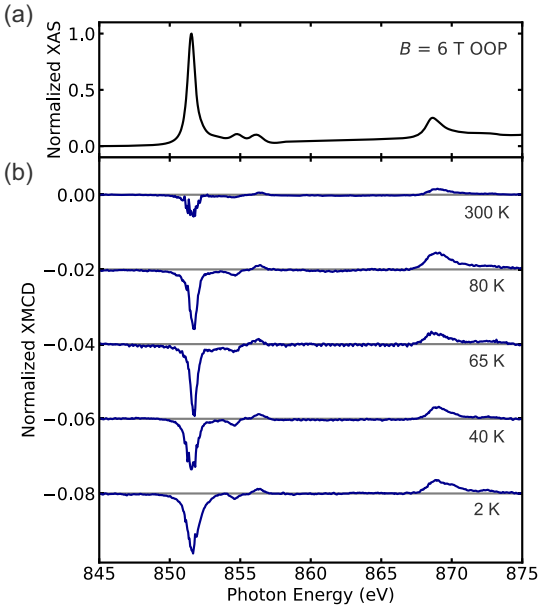

Figure 3. a) Normalized XAS sum spectrum measured at 2 K and b) temperature-dependent XMCD spectra at the Ni $L_{2,3}$ edge. All spectra were acquired at a fixed out-of-plane field of 6 T with incoming X-rays at normal incidence. The XMCD spectra have been vertically offset for clarity.

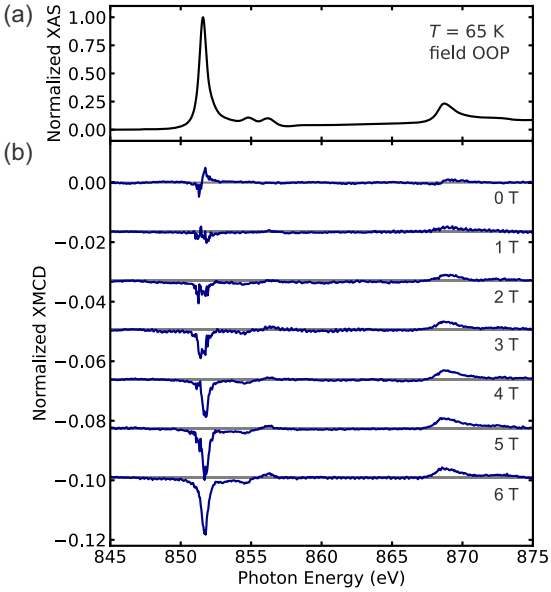

Figure 4. a) Normalized XAS sum spectrum at the Ni $L_{2,3}$ edge, measured at 65 K in an applied field out-of-plane field of 6 T. b) Corresponding XMCD spectra as a function of field from 0 T to 6 T. Measurements were performed at normal incidence of the X-rays, and the XMCD spectra are vertically offset for clarity.

near the surface. In addition to the reduction in XMCD intensity, an effect that may seem counterintuitive from the perspective of conventional ferromagnetic ordering, we also observe a gradual broadening of the spectral features below 59 K. In the monoclinically distorted low-temperature crystal structure, the various spins will feel slightly different exchange interactions, which can lead to slight shifts in energy, resulting in a broadened XMCD response. Although no XMCD studies on helimagnetic materials reporting similar broadening effects are currently known, related temperature-dependent changes in hybridization, localization, or magnetic interactions influencing the XMCD line shape have been observed in other 3*d* transition metal compounds. For example, XMCD studies on Co_2MnGe revealed multiplet features in the Mn $L_{2,3}$ spectra attributed to localized 3*d* electrons and temperature-dependent hybridization effects.[25] Likewise, in GdNi, strong hybridization between Ni 3*d* and Gd states leads to significant temperature-dependent changes in the XMCD spectral profile.[26]

Finally, we investigate the XMCD behavior in the intermediate antiferromagnetic phase between 59 and 75 K. **Figure 4** shows XMCD spectra acquired at 65 K in out-of-plane magnetic fields from 0 T to 6 T. To estimate the magnetization, we use the peak asymmetry, defined as the L_3 XMCD amplitude divided by the XAS sum intensity (see Supporting Information for ref. [27]). To determine the asymmetry values, we evaluated the XMCD amplitude for each field by identifying the minimum of the L_3 edge within a narrow energy window around the peak, rather than taking the value at a fixed energy, minimizing the influence of noise and slight peak shifts across the field-dependent spectra. From these data, we extract the average Ni magnetic moment along the field direction at each field value, which is plotted in **Figure 5**. The measurement at 0 T is excluded because it lacks

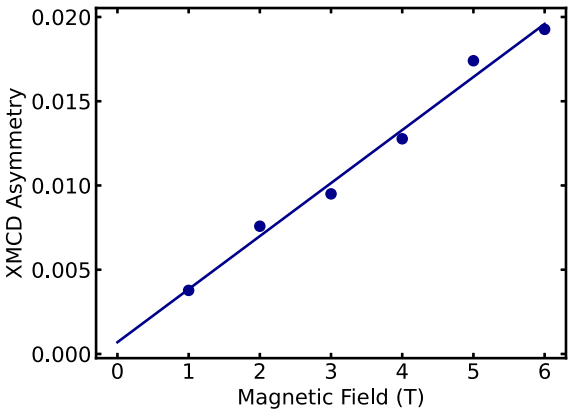

Figure 5. XMCD asymmetry (i.e., maximum peak XMCD divided by sum XAS) at 65 K as a function of the applied out-of-plane magnetic field. The data points (dots) are derived from the L_3 edges in the XMCD spectra shown in Figure 4. Note that the uncertainty in the asymmetry is expected to be greater at low fields due to reduced signal strength and less well-defined spectral features. The solid line represents a linear fit to highlight the nearly linear proportional relationship between magnetization along the field direction and magnetic field for fields up to 6 T.

a discernible ferromagnetic-like XMCD lineshape. The linear trend observed above 0 T is therefore extrapolated down to 0 T to emphasize the apparent proportionality between magnetization and applied field at 65 K. Similar behavior was observed for the same set of measurements for X-rays in grazing incidence.

Although NiI_2 hosts paramagnetic, antiferromagnetic and helimagnetic phases at low fields, we observe XMCD at all studied temperatures once the out-of-plane field is sufficiently large.

Above 75 K, the XMCD signal is due to the paramagnetic response, whereas between 59 and 75 K, there are ferromagnetically ordered Ni layers that are antiferromagnetically coupled over longer distances. The behavior of NiI_2 in this phase is similar to CrI_3—another vdW antiferromagnet—where the application of an out-of-plane magnetic field overcomes the weak antiferromagnetic interlayer coupling, resulting in ferromagnetic alignment of the layers[28] and a corresponding XMCD signature.[29] The absence of a sharp transition in the field dependence suggests that the interlayer antiferromagnetic coupling in NiI_2 is similarly weak and readily overcome by modest out-of-plane fields. While this field dependence may resemble a paramagnetic response, previous neutron and magnetometry studies place 65 K firmly within the antiferromagnetic regime, indicating that the XMCD signal arises from field-aligned spins in an antiferromagnetic background rather than a purely paramagnetic phase. The XMCD peak becomes less well defined below 2 T, increasing the uncertainty in the peak asymmetry ratio extraction in this field range. Accordingly, the uncertainty in the extracted asymmetry values is expected to be higher at low fields, though not quantified here due to the lack of an established method to uniquely determine error bars in this case. Although sum-rule integration offers an alternative for quantifying magnetic moments, the limited signal-to-noise ratio at low field renders it less reliable. We therefore chose the peak asymmetry ratio as a more consistent and robust metric for evaluating the field dependence of the XMCD response. Similarly, in the spin spiral state below 59 K, applying a strong enough magnetic field is expected to result in the formation of a conical helix.[30] Despite these indications, we observed no clear ferromagnetic-like XMCD at zero field for any temperature, suggesting that there is no net moment below some threshold field.

4. Conclusions

In summary, we have performed a detailed X-ray magnetic spectroscopy study on freshly cleaved NiI_2 single crystals, combining Ni $L_{2,3}$-edge XAS and XMCD with atomic multiplet calculations. We have demonstrated that the magnetism in NiI_2 is intrinsic and arises from a covalent Ni $3d$ ground state exhibiting a significantly reduced spin moment, rather than arising from metallic Ni or other extrinsic impurities. Comparison of the measured XAS and XMCD with multiplet calculations indicates a high spin ground state with 54.8% d^8, 43.4% d^9, and 1.8% d^{10} character, amounting to a d-count of $n_d = 8.47$. This is different compared to the more ionic NiO, which is closer to $n_d = 8$. It demonstrates that in NiI_2, there is a large charge transfer of electrons from the ligand iodide ions to the Ni cations. The resulting hole density on the I^- ions influences the magnetic behavior. In NiI_2, magnetic exchange interactions, particularly between first and third nearest neighbors, play a crucial role in determining its magnetic properties, leading to a helimagnetic state and multiferroicity, especially in its monolayer form. Our results show robust XMCD signals across all magnetic phases under applied out-of-plane fields, yet no intrinsic moment at zero field, confirming a field-driven spin alignment mechanism. Although NiI_2 has been confirmed as a 2D semiconducting multiferroic, its low transition temperature in the monolayer limit (≈21 K[5]) still represents a significant hurdle for device implementation. Future efforts should therefore focus on exploring doping strategies, strain engineering, or heterostructure fabrication to enhance its critical temperature and fully harness the rich magnetoelectric physics of NiI_2 for practical spintronic and multiferroic applications.

Acknowledgements

Experiments were performed at the BOREAS beamline at the ALBA Synchrotron (proposal 2022025699) with the collaboration of ALBA staff. T.H. acknowledges financial support from the Oxford-ShanghaiTech collaboration project and EPSRC (EP/X015793/1); G.v.d.L. from EPSRC (EP/X015599/1); E.L.A. from EPSRC (EP/W524311/1) and the Diamond Light Source; and E.H. from an STFC-Diamond-EPSRC studentship (project 2604894, EP/R513295/1, and EP/T517811/1). J.H. acknowledges support from the National Science Foundation under grant no. DMR-2238254 for sample synthesis.

Conflict of Interest

The authors declare no conflict of interest.

Author Contributions

Ethan L. Arnold: formal analysis (lead); investigation (supporting); software (lead); visualization (lead); writing—original draft (lead); and writing—review and editing (equal). **Emily Heppell**: data curation (lead) and formal analysis (equal); software (equal). **Rabindra Basnet**: methodology (equal). **Binshuo Zhang**: methodology (equal). **Jieyi Liu**: conceptualization (supporting) and funding acquisition (lead). **Javier Herrero-Martin**: data curation (supporting) and methodology (supporting). **Charles Guillemard**: data curation (supporting) and methodology (supporting). **Yanfeng Guo**: conceptualization (supporting) and supervision (lead). **Jin Hu**: conceptualization (supporting) and supervision (lead). **Dirk Backes**: data curation (supporting); supervision (lead); and writing—review and editing (equal). **Gerrit van der Laan**: conceptualization (equal); formal analysis (equal); funding acquisition (supporting); investigation (equal); methodology (lead); project administration (supporting); software (equal); supervision (lead); validation (lead); writing—original draft (equal); and writing—review and editing (equal). **Thorsten Hesjedal**: conceptualization (lead); data curation (supporting); formal analysis (supporting); funding acquisition (lead); investigation (supporting); methodology (lead); project administration (lead); resources (lead); supervision (lead); validation (equal); visualization (equal); writing—original draft (equal); and writing—review and editing (Lead). **Ethan L. Arnold** and **Emily Heppell** contributed equally to this work.

Data Availability Statement

The data that support the findings of this study are available from the corresponding author upon reasonable request.

Keywords

magnetic 2D materials, magnetic spectroscopy, X-ray techniques

Received: April 1, 2025
Revised: May 13, 2025
Published online:

[1] S. A. Wolf, D. D. Awschalom, R. A. Buhrman, J. M. Daughton, S. von Molnar, M. L. Roukes, A. Y. Chtchelkanova, D. M. Treger, *Science* **2001**, *294*, 1488.
[2] F. Matsukura, Y. Tokura, H. Ohno, *Nat. Nanotechnol.* **2015**, *10*, 209.
[3] K. S. Burch, D. Mandrus, J.-G. Park, *Nature* **2018**, *563*, 47.
[4] C. Gong, L. Li, Z. Li, H. Ji, A. Stern, Y. Xia, T. Cao, W. Bao, C. Wang, Y. Wang, Z. Qiu, R. Cava, S. G. Louie, J. Xia, X. Zhang, *Nature* **2017**, *546*, 265.
[5] Q. Song, C. A. Occhialini, E. Erge¸cen, B. Ilyas, D. Amoroso, P. Barone, J. Kapeghian, K. Watanabe, T. Taniguchi, A. S. Botana, S. Picozzi, N. Gedik, R. Comin, *Nature* **2022**, *602*, 601.
[6] H. Ju, Y. Lee, K.-T. Kim, I. H. Choi, C. J. Roh, S. Son, P. Park, J. H. Kim, T. S. Jung, J. H. Kim, K. H. Kim, J.-G. Park, J. S. Lee, *Nano Lett.* **2021**, *21*, 5126.
[7] D. Lebedev, J. T. Gish, E. S. Garvey, T. K. Stanev, J. Choi, L. Georgopoulos, T. W. Song, H. Y. Park, K. Watanabe, T. Taniguchi, N. P. Stern, V. K. Sangwan, M. C. Hersam, *Adv. Funct. Mater.* **2023**, *33*, 2212568.
[8] S. Son, Y. Lee, J. H. Kim, B. H. Kim, C. Kim, W. Na, H. Ju, S. Park, A. Nag, K.-J. Zhou, Y.-W. Son, H. Kim, W.-S. Noh, J.-H. Park, J. S. Lee, H. Cheong, J. H. Kim, J.-G. Park, *Adv. Mater.* **2022**, *34*, 2109144.
[9] M. A. McGuire, *Crystals* **2017**, *7*, 121.
[10] S. R. Kuindersma, J. P. Sanchez, C. Haas, *Phys. B+C* **1981**, *111*, 231.
[11] T. Kurumaji, S. Seki, S. Ishiwata, H. Murakawa, Y. Kaneko, Y. Tokura, *Phys. Rev. B* **2013**, *87*, 014429.
[12] H.-S. Yu, X.-S. Ni, D.-X. Yao, K. Cao, *Phys. Rev. B* **2025**, *111*, 094440.
[13] F. Y. Gao, X. Peng, X. Cheng, E. Viñas Boström, D. S. Kim, R. K. Jain, D. Vishnu, K. Raju, R. Sankar, S.-F. Lee, M. A. Sentef, T. Kurumaji, X. Li, P. Tang, A. Rubio, E. Baldini, *Nature* **2024**, *632*, 273.
[14] J. H. Kim, T. S. Jung, Y. Lee, C. Kim, J.-G. Park, J. H. Kim, *Phys. Rev. B* **2023**, *108*, 064414.
[15] S. Wu, X. Chen, C. Hong, X. Hou, Z. Wang, Z. Sheng, Z. Sun, Y. Guo, S. Wu (Preprint), arXiv:2307.10686, v1, Submitted: Jul. **2023**.
[16] G. van der Laan, A. I. Figueroa, *Coord. Chem. Rev.* **2014**, *277–278*, 95.
[17] B. T. Thole, P. Carra, F. Sette, G. van der Laan, *Phys. Rev. Lett.* **1992**, *68*, 1943.
[18] G. van der Laan, B. T. Thole, *Phys. Rev. B* **1991**, *43*, 13401.
[19] G. van der Laan, *Lect. Notes Phys.* **2006**, *697*, 143.
[20] R. D. Cowan, *The Theory of Atomic Structure and Spectra*, University of California Press, Berkeley **1992**.
[21] G. van der Laan, J. Zaanen, G. A. Sawatzky, R. Karnatak, J.-M. Esteva, *Phys. Rev. B* **1986**, *33*, 4253.
[22] G. van der Laan, C. M. B. Henderson, R. A. D. Pattrick, S. S. Dhesi, P. F. Schofield, E. Dudzik, D. J. Vaughan, *Phys. Rev. B* **1999**, *59*, 4314.
[23] G. van der Laan, B. T. Thole, *J. Phys.: Condens. Matter* **1992**, *4*, 4181.
[24] G. van der Laan, *Phys. Rev. B* **1998**, *57*, 112.
[25] J. Grabis, A. Bergmann, A. Nefedov, K. Westerholt, H. Zabel, *Phys. Rev. B* **2005**, *72*, 024437.
[26] C. W. Chuang, H. J. Lin, F. M. F. de Groot, F. H. Chang, C. T. Chen, Y. Y. Chin, Y. F. Liao, K. D. Tsuei, J. Arout Chelvane, R. Nirmala, A. Chainani, *Phys. Rev. B* **2020**, *101*, 115137.
[27] E. L. Arnold, J. M. Riley, L. B. Duffy, A. I. Figueroa, R. Held, K. M. Shen, D. G. Schlom, P. D. C. King, M. Hoesch, G. van der Laan, T. Hesjedal, *Phys. Rev. Mater.* **2025**, *9*, 024410.
[28] S. Jiang, J. Shan, K. F. Mak, *Nat. Mater.* **2018**, *17*, 406.
[29] A. Frisk, L. B. Duffy, S. Zhang, G. van der Laan, T. Hesjedal, *Mater. Lett.* **2018**, *232*, 5.
[30] M. Mostovoy, *Phys. Rev. Lett.* **2006**, *96*, 067601.